



<http://www.diva-portal.org>

Postprint

This is the accepted version of a paper published in *Tectonophysics*. This paper has been peer-reviewed but does not include the final publisher proof-corrections or journal pagination.

Citation for the original published paper (version of record):

García Juanatey, M., Hübner, J., Tryggvason, A., Juhlin, C., Pedersen, L B. et al.
(2019)
2D and 3D MT in the central Skellefte Ore District, northern Sweden
Tectonophysics
<https://doi.org/10.1016/j.tecto.2019.04.003>

Access to the published version may require subscription.

N.B. When citing this work, cite the original published paper.

Permanent link to this version:

<http://urn.kb.se/resolve?urn=urn:nbn:se:uu:diva-178057>

2D and 3D MT in the central Skellefte Ore District, northern Sweden

María A. García Juanatey^{a,*}, Juliane Hübert^{a,b}, Ari Tryggvason^a,
Christopher Juhlin^a, Laust B. Pedersen^a, Tobias E. Bauer^c, Mahdiah
Dehghannejad^{a,d}

^a*Uppsala University*

^b*Now: British Geological Survey*

^c*Luleå University of Technology*

^d*Now: Ramboll Sweden*

Abstract

New broadband magnetotelluric (MT) data have been acquired along two parallel profiles in the central part of the metallogenic Skellefte district in northern Sweden. The data were recorded as part of the *Swedish 4D modelling of mineral belts* project and cover an area with several economical and sub-economical deposits. The dimensionality and quality of the data were carefully analyzed and new error floors were systematically determined prior to inverse modelling in 2D and 3D. The algorithms used were EMILIA and WSINV3DMT. For the 2D inversion, only the determinant of the impedance tensor was used, while for the 3D inversion all elements were considered. The obtained models fit the inverted data, and image the main regional features. A detailed comparison reveals the superiority of the 3D model, both in model structures and data fit. After assessing the main features in the model, an interpretation is proposed and refined with the support of previous geophysical studies. The most interesting features are large and medium-sized conductors associated with crustal-scale shear zones and faults within the Skellefte Group rocks. These may be depicting a network of fossil pathways for hydrothermal fluid transport and as such, provide new insight into past processes in the area.

*Corresponding author

Email address: maria.garcia@geo.uu.se (María A. García Juanatey)

1. Introduction

The Skellefte district is a Palaeoproterozoic volcanic arc in northern Sweden, rich in volcanic-hosted massive sulphide deposits. The main metals produced in the area are zinc, copper, lead, silver, tellurium and gold. Given that the district has been mined for over 100 years, and shallow deposits are being depleted, the requirements of today are to locate deeper targets. In order to accomplish this, a better understanding at the regional scale is necessary (Weihed, 2010). To address this challenge, the project *Swedish 4D modelling of mineral belts* was launched in 2008. Its main purpose was to unravel the regional structures and tectonic setting of the district, through 3D modelling of the present geological structure, and conceptual models of their evolution.

In the framework of this project, new geophysical and geological data were acquired in the district, mainly in two key localities: to the west, in the surroundings of the Kristineberg mine, and in the central part of the district, where the survey here described is located (see Figure 1). The geophysical investigations include seismic reflection, broadband magnetotellurics (MT), and potential field data acquisition (locations of the seismic profiles and MT sites across the district are shown in Figure 1).

The most relevant studies for the current study are: three seismic reflection profiles (Dehghannejad et al., 2012a), potential field modelling along the seismics (Tavakoli et al., 2012a) and geo-electrical surveys (Tavakoli et al., 2012b, 2016a) in the central part of the district. Also pertinent are 2D and 3D MT surveys in the Kristineberg mining area (see Figure 1 for the location of MT sites across the district; Hübner et al., 2009; García Juanatay et al., 2013a,b; Hübner et al., 2013).

In this paper, we present previously unpublished MT data from the Mauriliden area, as well as data analysis and selected methodology. The results derived from 2D and 3D inversion are also shown together with a geological interpretation of the 3D resistivity model, and further discussion and integration with other geophysical studies in the area.

2. Geological background

Rock-types in the Skellefte district comprise metamorphosed Palaeoproterozoic supracrustal and intrusive rocks that formed in a volcanic arc setting (Figure 1). The oldest known supracrustal rocks in the district are bimodal volcanic rocks of the 1.9-1.89 Ga Skellefte Group (Figure 2; Allen et al., 1996; Weihed et al., 2005; Skyttä et al., 2011). They consist mainly of rhyolitic volcanic and volcanoclastic rocks with minor occurrences of basalts, andesites

and dacites (Allen et al., 1996). Skellefte Group rocks are unconformably to conformably overlain by sedimentary rocks of the Vargfors Group. Sedimentary stratigraphy in the northern parts of the study area consists of turbiditic mudstones and sandstones unconformably overlain by monomict and polymict conglomerates, whereas the Vargfors Group in the southern part of the area is dominated by solely turbiditic mudstones with minor sandstone reinterbeds (Dumas, 1986; Bauer et al., 2011, 2013). An intercalated ignimbrite constrains the sedimentation age to 1875 ± 4 Ma (Billström and Weihed, 1996). The uppermost part of the Vargfors stratigraphy is marked by Gallejaur-type mafic volcanic rocks. Locally the Vargfors Group mafic volcanic and volcanoclastic rocks occur within high-strain zones (Bauer et al., 2013).

Intrusive rocks in the central Skellefte district are dominated by the 1.89-1.97 Ga first phase (GI) of the poly-phase Jörn intrusive complex, with heterogeneous compositions ranging from tonalite to granodiorite with mafic enclaves (Wilson et al., 1987; González-Roldán, 2010). To the north, the district is bounded by mainly felsic volcanic rocks of the Arvidsjaur Group. To the south, and east the district is bordered by metasedimentary rocks of the Bothnian Supergroup, suggested to be the basement for the Skellefte district (Rutland et al., 2001; Weihed et al., 2002; Skyttä et al., 2012), whereas the border to the Vargfors Group was drawn arbitrarily on the map (Kathol and Weihed, 2005) with a transition into Bothnian Supergroup metasediments. To the west and partly to the south the Skellefte district is bordered by 1.82-1.78 Ga late- to post-tectonic intrusive rocks of the Transscandinavian Igneous Belt (TIB, Kathol and Weihed, 2005).

The structural geometry of the central Skellefte district is dominated by a distinct pattern of syn-extensional, NNW-SSE striking, listric normal faults and associated NE-SW striking, sub-vertical transfer faults (Bauer et al., 2011; Dehghannejad et al., 2012a). Subsequent crustal shortening from SSW at 1.87 Ga resulted in fault inversion and upright folding (Bauer et al., 2011; Skyttä et al., 2012). Successive E-W crustal shortening at 1.82-1.80 Ga (Weihed et al., 2002) was accommodated by pre-existing regional-scale N-S striking shear zones (Bergman Weihed, 2001) and hence did not cause folding in the study area.

The volcanic-hosted massive sulphide (VHMS) deposits in the Skellefte district formed as mainly sub-seafloor replacement within volcanoclastic sedimentary rocks in the uppermost part of Skellefte Group stratigraphy (Allen et al., 1996). The VHMS-deposits (see Figure 2) are suggested to be structure-controlled utilizing the syn-extensional faults as fluid conduits (Allen et al., 1996; Bauer et al., 2014). During the 1.87 Ga basin inversion, the VHMS-deposits were transposed into their current day, predominantly steep orien-

tations (Bauer et al., 2011, 2014).

3. Data acquisition and processing

In fall 2010, 34 broadband MT sites were installed in the central Skellefte district, nearby the Maurliden mine. The site spacing ranged between 1 and 2 km along two profiles 3 to 4 km apart and ~ 23 km long. The NNE - SSW orientation of the profiles was chosen to be perpendicular to the main structural trend in the geology (see Figure 2). Both profiles start on top of the Jörn granite to the north, cross the surfacing corridor of the Skellefte volcanics, and finish on top of mudstone and sandstones of the Vargfors Group, very close to TIB related intrusions.

During data acquisition, all five MT channels, three components of the magnetic field and two horizontal components of the electric field, were recorded with two different sampling rates: 1000 Hz for two hours at midnight and 20 Hz for one or two days continuously. The instrumentation consisted of non-polarizable Pb/PbCl electrodes from Uppsala University (Sweden), induction coils MFS05 and MFS06 from Metronix (Germany) and LEMI120 from Ukraine. All measurements were synchronized with GPS clocks.

The data processing and estimation of the MT transfer functions, was carried out with the MTU2000 algorithm of Smirnov (2003). Multi-site processing with a remote reference site provided stable transfer functions in the frequency range of 700 Hz to 200 s. Most of them show decreasing apparent resistivities, with increasing periods, from 10^4 to 10^2 $\Omega\cdot\text{m}$, while phases increase from $\sim 40^\circ$ to 80° (see Figure 3). This pattern is very similar to that observed on the data to the west of the district (Hübert et al., 2009; García Juanatey et al., 2013a,b), indicating a common regional structure.

4. Data quality check

Along the two profiles, the data quality varies from good to noisy. Some stations present significant disturbances in one component, but not in the other. The most probable source of noise is the multiple high-voltage power lines that cross the area of investigation, distributing the electric power generated at the south of the Vargfors dam. Additionally, the galvanic coupling of the electrodes was difficult at some sites due to frozen ground.

To address this situation, we chose to perform a systematic quality check of the data set. A common procedure in 2D studies is to test the consistency of apparent resistivity and phase through the dispersion relations, as inconsistencies could be caused by low data quality (Parker and Booker, 1996). However, it has been shown that dispersion relations can also break down

due to multidimensional resistivity structures (Weidelt and Kaikkonen, 1994; Berdichevsky and Pokhotelov, 1997; Alekseev et al., 2009) and hence, are not an optimal tool to evaluate data in 3D environments. Nevertheless, they provide means to identify in an objective manner potentially noisy data. Thus, we decided to make use of this tool followed by a visual inspection of the data curves.

To test that the dispersion relations are met, we performed 1D inversions of both apparent resistivity and phase of each off-diagonal element and the determinant of the impedance tensor (e.g. Smirnov and Pedersen, 2009). The the root mean square (RMS) of the best fitting 1D model is then an indicator of the validity of the dispersion relations. Note that all the RMS values in this study are related to misfits normalized by the assumed errors. For simplicity, prior to inversion we assumed relative errors of 1% on the impedances. Thus, an RMS of X indicates that the obtained model fits the data within relative errors of X%.

Table 1 summarizes the values obtained for each impedance element. For the off-diagonal elements half of the values are below 5% and about a quarter above 20%. After a visual inspection of all elements with RMS values above 20%, we decided to reject those with RMS 100% or higher and Zyx of site A07 (RMS 64.3), since they showed erratic behaviour. Other inspected components were deemed worth keeping although with increased error floors. In the case of the determinant data, the values are between 30% and 40% for most sites, with values from profile B somewhat higher, and above 50% for eight of them. The latter were rejected after visual inspection. As expected, the discarded sites coincide with those in which one off-diagonal component is very noisy.

The 1D RMS values shown in Table 1 reflect the variability of data quality. To ensure that each component has errors that express the level of confidence we have on the data prior inversion, we assigned the obtained 1D RMS values, if greater than 5%, as new relative error floors on the impedance on top of the original errors. Sites A14 and A18 were exempted from this procedure as their high RMS values might be due to off-quadrant phases and not to problems with the data quality. Components with 1D RMS values lower than 5%, together with sites A14 and A18, were subject instead to a 5% error floor. For the determinant, we did not consider it necessary to calculate new error floors as the 1D RMS values are very similar within each profile.

It is possible that this scheme for calculating error floors may lead to damping of 3D effects. Nevertheless, it provides an objective way to set error floors for the impedance elements, which is commonly done in a more subjective fashion.

5. Strike and dimensionality analysis

To assess the dimensionality of the resistivity structures in the study area, and potentially find a preferred geoelectrical strike direction, we first looked at rotational invariants like Swift's skew (Swift, 1967) and Bahr's phase sensitive skew (Bahr, 1988, 1991), then at strike estimates from the impedance tensor (Bahr, 1991; Zhang et al., 1987), and finally at the induction arrows from the tipper vector.

Figure 4 shows Swift's skew and Bahr's phase sensitive skew for all sites excluding those with very noisy components (i.e. sites A07, A09, A12, A17, B05 and B06, see section 4). The values for both skews are rather high, indicating deviation from a simple 2D anomaly and/or galvanic distortions (Swift's skew), and deviation from a superimposition model with local 3D anomalies (Bahr's skew). Bahr (1991) suggested a threshold of 0.3 for the phase sensitive skew above which the data could only be explained with 3D anomalies (red line in Figure 4), which is the case for a great number of our data points.

Even though the resistivity structures in the study area seem to be of a 3D nature, we investigate further the possibility of a 2D approximation. Using the approach outlined by Zhang et al. (1987), it is possible to estimate strike directions, although with 90° ambiguity, from the impedance tensor taking into account galvanic distortions. Figure 5 shows a rose plot with the calculated strike angles for each site and period. The estimates were obtained averaging three sites and one decade in period to reduce large strike variability. The rose plot shows a somewhat broad but clear direction at ~40° (or ~130°), not far from the lithological strike of 115° observed with the surface geology.

An indication of how certain these estimates are can be obtained through their associated misfits (\sqrt{Q} in Zhang et al., 1987), shown in a histogram in Figure 6. A value of one indicates that the data point fulfills 2D conditions under the estimated strike direction within the assumed errors. As can be seen, even though many of the data points have low \sqrt{Q} values, most of them would still require higher errors to comply with 2D assumptions.

An additional indication of dimensionality is the orientation of the real induction arrows of the tipper vector. With the Wiese convention (Wiese, 1962) the arrows point away from conductive features and on ideal 2D settings they are perpendicular to the strike direction. Figure 5 shows a rose plot of the orientation of the arrows for all sites and periods. From this Figure it is evident that the arrows have a clearly predominant north-south direction, indicating a geoelectrical strike in the east west direction at all sensed depths. The difference to the previously estimated strike angles from

the impedance tensor ($\sim 130^\circ$) is about 30° . This deviation has also been observed in the Kristineberg area 50 km to the west (García Juanatey et al., 2013a), where joint inversion of the impedance tensor and the induction arrows could not be performed successfully. It is not clear what gives rise to such a difference on the strike estimates, but its geographical spread across the district and further to the north (see Cherevatova et al., 2015), suggests that it might be related to a regional-scale feature.

We conclude that even though the rotational invariants show that the data set deviates from necessary 2D conditions, the strike analysis of the impedance tensor and the direction of the induction arrows supports the possibility of a 2D approximation of the resistivity structures if higher errors are assumed. Given that 2D and 3D inversion of MT data have particular advantages and disadvantages of their own, and to some extent complement each other (Hübner et al., 2013), we decided to carry out both.

6. Inversion

6.1. 2D inversion

The data set was inverted in 2D using EMILIA (Kalscheuer et al., 2010). Only the determinant of the impedance tensor was inverted as it is less sensitive to 3D effects (Pedersen and Engels, 2005) and has already given good results in previous studies within the Skellefte District (Hübner et al., 2009; García Juanatey et al., 2013a,b).

Site locations were projected on two straight lines with azimuth of 25° (see Figure 2). As discussed in section 4, noisy transfer functions were rejected leaving gaps along the profiles (see Table 1 and Figure 2). Seven frequency estimates per decade were inverted with a single global error floor of 5% on the impedances. The models were discretized with cells of fixed horizontal length of ~ 250 m, and increasing vertical length starting at 50 m. First, for each profile a preliminary inversion with an OCCAM scheme (Constable et al., 1987) was performed using a homogeneous halfspace with a resistivity of $1000 \Omega\cdot\text{m}$ as the initial model. Then, the resulting models were used as starting models for a subsequent inversion to reduce the data misfit with a damped OCCAM approach using Marquardt-Levenberg damping (Yan et al., 2017, e.g.). This procedure rendered stable resistivity models with a data misfit RMS of 1.26 and 1.60 for profile A and B, respectively. Models are shown in Figure 7 and the data fit for selected sites in Figure 3. The models share regional features as it would be expected for parallel profiles perpendicular to the geological strike, but they also show strong local variations.

The most striking differences are at the top 3 km towards the south, where profile A shows very high conductivities while B very high resistivities (CI and RI), and below 4 km depth to the north, where resistivities decrease with depth in profile A, but remain fairly constant at $\approx 10000 \Omega\cdot\text{m}$ in profile B. Common features are the high resistivities ($\approx 1000 \Omega\cdot\text{m}$) that extend from the surface down to 2 and 10 km depth. These resistive features are interspersed by resistivities below $1000 \Omega\cdot\text{m}$. Along profile A, below site A06 and in a larger portion at the center of profile B, the resistivities drop further to reach $100 \Omega\cdot\text{m}$ (IC). Below the resistive features the resistivities decrease with depth in both models, except at the north of profile B, as mentioned earlier. This decrease in resistivity is also observed in western Skellefte, although at a shallower depth (4-6 km). At the southern end of both profiles the resistivities are much lower, below $100 \Omega\cdot\text{m}$ and sometimes below $1 \Omega\cdot\text{m}$. These low resistivities extend from the surface in A, and from 3 km depth in B, to more than 20 km depth in both profiles.

Looking in more detail to the resistivity variations at the surface and considering previous studies in the mining district (i.e. García Juanatey et al., 2013a; Hübert et al., 2009), it is possible to make a preliminary correlation between the model features and the main lithological groups. The Jörn intrusion can be associated to the strong resistors at the north of both profiles (RN), and it seems to reach greater depths along Profile B. The rocks of the Skellefte Group seem to be related to both very resistive (e.g. RS and RC) and moderately resistive features. The strong contrast between both profiles at the south (CI and RI) might be due to localized graphitic shales from the Bothnian Supergroup.

6.2. 3D inversion

The 3D inversion was carried out with the data space inversion code WSINV3DMT (Siripunvaraporn et al., 2005). It allows the inversion of the full impedance tensor, including the diagonal elements, but not of the tipper vector (academic license). The code has been previously employed with data from the Skellefte District, to the west of our current study, and produced good results (see Hübert et al., 2013).

The admitted model discretization is a rectangular grid parallel to the north-south and east-west direction. Since the site locations are approximately aligned along two profiles with azimuth 25° , we considered rotating the data to permit a coarser cell size in the direction perpendicular to the profiles. However, a rotation of the data set would also mix the errors of the different components of the impedance tensor, and as it can be seen from Table 1 these errors can be quite different. Thus, to preserve the components

with high data quality and down weight the others as suggested in section 4, it is necessary to invert the unrotated data set.

The finally chosen model discretization consists of a horizontal cell size of 500x500 m, and an increased vertical size starting at 30 m (see Figure 8). Site locations were slightly shifted (≈ 250 m) to coincide with the centers of the cells, and in a few cases, they were shifted further to allow one more cell between sites (see Figure 8).

We inverted the full impedance tensor of all included sites, with four period estimates per decade. The assumed error floors are described in section 4 and Table 1. The followed inversion strategy was the same as described by Hübert et al. (2013). We carried out a first inversion with a homogeneous halfspace of 1000 $\Omega\cdot\text{m}$ as initial and prior model. Then, the best fitting obtained model (RMS 5.43) was used as initial and prior model of a subsequent inversion. This produced a model able to fit the input data reasonably well (data misfit RMS 2.64). Figure 9 shows the RMS of the data misfit for each site and it can be seen that although several sites have an RMS close to the total one, most values are smaller. This is because there are three outliers (sites A06, A11 and A14) that have significantly higher RMS (≈ 4). These sites are scattered along profile A and do not indicate a systematic bias in the model. The sources for such high RMS on those sites can be due to the existence of very localized structures, galvanic distortions or inadequate error bounds. It is worth noting, that in contrast, site A12 has an excessively low RMS (0.01), most likely due to too large error bounds. An additional sample of the data fit of the model is shown as apparent resistivity and phase for selected sites in Figure 3, together with the responses of the 2D models.

The resulting model, displayed in Figures 7, 10, 11, and 12, is rich in structures with alternating fairly extreme resistivities, mostly between 1 and 10^5 $\Omega\cdot\text{m}$. Consistently, several of the structures present a strike close to 130° as estimated with the strike analysis from the impedance tensor in section 5. In an attempt to obtain a smoother model, we tested inversions with larger model scale lengths for the model covariance (time steps 7 and 10). The resulting models were either not able to fit the data to the same level, or were similarly rough. Thus, we decided to keep the model obtained with the default scale lengths (time step 5). In the following, we attempt to describe the model by highlighting the most prominent features. To simplify this task, we grouped neighboring conductors with trends similar to the mentioned strike. Features shallower than 250 m are disregarded as they are too shallow to be well resolved given the coarse site spacing.

Considering the conductors (1 to 100 $\Omega\cdot\text{m}$), there are four parallel groups with the previous mentioned strike. Close to the center from about 500 m depth, there are two aligned conductors that get successively deeper towards

the southeast (CTII in Figures 10.c, 10.d and 11.c). Another group consists of two conductors to the north, spanning from about 500 m to 2 km depth (CTIII in Figures 10.c and 11.a). Between CTII and CTIII and from 1 km to 6 km depth, there is a conductor that branches into a less conductive anomaly (CTIV in Figures 10.d and 11.b). The fourth group is at the northeastern corner of the model with its top at about 6 km depth (CTVI in Figures 10.e, 10.f and 7 bottom right).

Other interesting conductors are: CII, from the surface to 1 km depth next to site B17 (Figure 10.b); CIII, a big near vertical conductor to the west of site A11 with resistivities below $1 \Omega \cdot \text{m}$ and extending deeper than 16 km; and CTV, a group of two big conductors at the southern end of the model, extending from 1 and 3 km to 15 km depth (Figures 10.d, 10.e and 11.d).

The already described conductive regions are surrounded by features with high resistivities ($\geq 10^4 \Omega \cdot \text{m}$). We divide them somewhat arbitrarily into five parts: RN to the north, an elongated resistor in the strike direction extending from 1 to 9 km depth (see Figure 10.c to 10.e); RC at the center, extending from the surface to 9 km depth and bounded to the south and north by CTII and CTIII (see Figure 10.c to 10.e); RS to the west, extending from the surface to 7 km depth (see Figure 10); RIII to the southeast, from the surface to 5 km depth (see Figure 10.c); and RI to the south, also observed in Model B, extending from the surface to 4 km depth plunging to the southeast (see Figures 10.b and 10.d). Below the high resistivities, from about 10 km depth, the model is dominated by more conductive values ($\leq 300 \Omega \cdot \text{m}$).

6.3. 3D model assessment

We tested the robustness of the conductive features in the obtained 3D model through constrained inversions. To do so, we removed each feature in turn from the 3D model. To avoid the introduction of new box-like structures, we selected a model region containing a particular conductive feature and replaced all resistivities below $1000 \Omega \cdot \text{m}$ with this value. The modified models were then used as initial and prior models for new 3D inversions. The new inversions produced models with similar and lower RMS than the original 3D model.

Analyzing the models with comparable RMS, we observe that for the most extensive features CIII and CTV, the low resistivities are recovered although with somewhat higher values (minimum values between 3 and $30 \Omega \cdot \text{m}$ instead of below $1 - 10 \Omega \cdot \text{m}$). The structures are fairly similar as in the original model but there are slight changes in position. CIII appears 350 m deeper and CTV plunges more towards the north than northeast. Comparing the new models and the original one site by site, one sees that in the case of CTV several sites to the south still show consistently higher RMS values. We

conclude then that both CIII and CTV are required by the data, although they might not be accurately resolved, hence the variability in position.

For the smaller features CTII, CTIII, CTIV and CTVI, the low resistivities are only partially recovered with values below $1000 \Omega\cdot\text{m}$ but higher than $300 \Omega\cdot\text{m}$, except in the case of CTIII where resistivities reach $100 \Omega\cdot\text{m}$. However, a site by site comparison of the RMS values, show that at least two sites nearby each tested feature fit the data worse than the original model. Looking at the new models in detail, it is also possible to see that the high resistivities surrounding the tested features are even higher than in the original model. Thus, we conclude that these conductive features are also necessary to fit the data, although they seem to be less resolved than CIII and CTV and might actually not be as conductive as in the original model.

Considering that moderate resistivity values are easier to interpret and noting that removing conductive values increased the resistivities surrounding them in the 3D model, we decided to test if it is possible to bound the resistivity values tighter in the 3D model, and still fit the data to the same level. To do so, we modified the 3D model by cutting off the highest resistivity values to $10^4 \Omega\cdot\text{m}$ and the lowest to $100 \Omega\cdot\text{m}$. This model was then again used in a new inversion as initial and prior model. The inversion produced a new 3D model with RMS 2.62, which is similar to that of the original 3D model (2.64). The structures within the new model are very similar to the original ones but the resistivity values are somewhat less diverse, lying mainly between 10 and $50000 \Omega\cdot\text{m}$ (although CIII and CTV still show resistivities below $10 \Omega\cdot\text{m}$ at their cores) instead of 1 and $300000 \Omega\cdot\text{m}$. These results indicate that the most extreme resistivity values of the original model can explain the data, but are not necessary to do so.

6.4. Comparison between 2D and 3D models

Figure 7, bottom, shows two vertical slices from the 3D model along the locations of profiles A and B. The 2D models are very smooth while the 3D model is very rich in structures. Nonetheless, several features are common to both 2D and 3D models, implying that these structures are fairly robust and relatively well resolved.

For example, a close look reveals that the resistive structures are very similar in the 2D and 3D models, although they are not exactly at the same locations or with the same dimensions. The largest discrepancies are: RN is shallower in Model A while in Model B it is further to the north and much more extensive than in the 3D model; RI extends deeper into the 3D model and is located further to the south; and RC in the 3D model seems to encompass several resistors from Model B. In the upper part (top 4 km), both the 2D and 3D models show conductive features intercalated

between the resistors. However, the resistivity values shown in the 2D models (100 - 1000 $\Omega\cdot\text{m}$) are significantly higher than in the 3D model (1 to 100 $\Omega\cdot\text{m}$). Regarding deeper parts (≥ 10 km depth), the 3D model shows very low resistivities while the 2D models only show a diffuse transition from high to low values with a conductive core to the south. This core and the shallower low conductivities at the south of the 2D models seem to be a distorted two dimensional representation of the sub-vertical conductors CTV from the 3D model (only partially visible on the slices shown in Figure 7).

To be able to compare the data fit between the 2D and 3D models we recalculated the RMS of the 2D forward responses against the full impedance tensor, as it was done with the 3D responses. The resulting value is 11.52 which is much higher than the RMS of the 3D model (2.64). Additionally, Figure 3 shows the data fit of all impedance elements of the 3D model together with the rotated forward responses of all impedance elements of the 2D models (the used rotation angle was -25° to match the direction of the data inverted in 3D). From this figure, it is also possible to observe that the data fit of the 3D resistivity model is superior to any of the 2D models, especially for sites with off-quadrant phases (e.g. site B19). As expected, the diagonal elements from the 2D models present the poorest data fit.

From the RMS values and Figure 3, we conclude that the 3D model is able to reproduce the observed data much better than any of the 2D models. Thus, we decide to rely on the 3D model for the following geological interpretation. It is important to keep in mind that, even though the chosen 3D model fits the data best, it is just one solution to an under-determined problem. Therefore, we base our interpretation on the features that have been found to be robust in the sensibility analysis (section 6.3) and the comparison above with the 2D models.

7. Interpretation

In the following section, we will interpret the most prominent features of the 3D resistivity model. First, we will focus on the shallower features of the model (upper 10 km), grouping them according to their associated lithological unit. Later on, we will consider the larger conductive anomalies that reach the deeper parts of the model. Since the northwestern and southeastern corners of the 3D model are not well resolved, we only interpret model features that are within a ~ 15 km wide band oriented SW-NE and enclosing the MT sites.

7.1. Skellefte Group

The upper 10 km of the 3D model is dominated by highly conductive and resistive features, CTII, CTIII, CTIV, RN, RC and RS (RIII is discussed later). These are aligned with the geological strike direction and are probably depicting the metavolcanic rocks from the Skellefte Group. The occurrence of extreme and opposite conductivity values within the Skellefte Group has also been observed in previous studies to the west of the current study area (García Juanatey et al., 2013a; Hübner et al., 2013). As in those studies, we attribute the highly conductive structures to hydrothermally altered volcanic rocks related to the ore deposits in the area, and the very high resistivities to the unaltered rocks hosting them. As a supporting fact for hydrothermally enhanced conductivities, two of the conductive anomalies can be associated with the surface expression of subvertical structures. As these syn-extensional structures acted as hydrothermal fluid conduits, the faults represent zones with more intense hydrothermal alteration compared to the generally less altered surrounding rocks. CTII aligns with the NE-SW striking Mauriliden-Finnliden (M-F) fault, and CTIII is intersected by one or more of the syn-extensional faults to the north of the study area. In the case of CTIV, there is no direct field observation of a fault related to it, but it aligns with the Skellefte river and the Vargfors dam and it is likely that another NE-SW striking fault subparallel to M-F runs along these features (see map on Figure 2). This group of conductive and resistive anomalies extends to about 10 km depth, supporting the notion of a thick package of volcanic rocks in this area. Their lateral extension is bounded to the north by a different resistivity pattern (discussed below) and to the south by the CTV conductors, although they might continue further south as the resistor RI. To the east and west the 3D model is unconstrained, and it is known from field observations that the Skellefte Group extends further in both directions.

7.2. Jörn intrusion

The northeastern corner of the 3D model down to 6 km depth is dominated by an heterogeneous region of several small features with different resistivity values (Figures 10.b to 10.d). This region seems to depict the GI-phase of the Jörn intrusion. The resistivities vary mostly between 100 and 1000 $\Omega\cdot\text{m}$, with some transgressions to more resistive values like in the case of RII. The great variations of conductivity can be due to the heterogeneous composition of the Jörn intrusion (see section 2). The southwestern contact of the intrusion is clearly delineated by the homogeneous resistor RN, attributed to a shear zone along the contact between the intrusion and volcanic rocks. This shear zone is characterized by multiple emplacements of mafic volcanic and sub-volcanic material (Bauer et al., 2013, c.f.). The

contact is very steep and dips towards the north down to 4 km, where it becomes vertical. Bauer et al. (2013) interpreted this contact as a break-back fault related to the 1.87 Ga compressional phase. At about 6 km depth, the intrusion is bottomed by the enhanced conductivities of CTVI.

7.3. *Post-orogenic intrusions, TIB*

The locations of features CII and RIII, to the south and east of sites B15 and B17 (Figure 10.b), correlate nicely with the TIB intrusions outlined on the geological map (Figure 10.a, please note that these outlines come mainly from magnetic lineaments). The gabbro seems to be conductive with resistivities between 1 and 300 $\Omega\cdot\text{m}$ (CII). It extends from the surface to about 1 km depth, becoming narrower at the bottom. The granitoid of Revsund type, shows up instead as a resistor with resistivities higher than 3000 $\Omega\cdot\text{m}$ (RIII). This value is in agreement with observations from previous MT studies in the district (Hübert et al., 2009; García Juanatey et al., 2013a; Hübert et al., 2013). It extends to 5 km depth. The lateral extension of the granite is unknown to the north, where it has a similar resistivity to the unaltered volcanic rocks, and to the east and south, where there are no MT sites and the model is poorly constrained. However, its contact to the west is clearly defined due to the resistivity contrast with the TIB gabbro (CII), and it dips to the west. It is possible that the southernmost resistor RI (Figures 10.c and 10.d), next to site B19 and extending to 2 km depth, is indicating the presence of more Revsund type intrusions below the metasedimentary rocks. However, as mentioned earlier, this resistor could be related to metavolcanic rocks of the Skellefte Group instead. Unfortunately, neither hypothesis can be verified or discarded with the available data.

7.4. *Large conductors*

The 3D resistivity model contains large, nearly vertical conductive features (CIII, CTV and CTVI) that extend beyond 12 km depth, and a deep conductive region ($\sim 100 \Omega\cdot\text{m}$) that connects with these conductors (Figures 10.e, 10.f, 11.c and 11.d).

The enhanced conductivity at depth that extends laterally throughout the area, indicates that the rocks underlying the Skellefte Group are fairly conductive. This is in good agreement with previous geological and geophysical studies in the district that propose that metasedimentary rocks of the Bothnian Supergroup represent the basement of the Skellefte Group (Rutland et al., 2001; Weihed et al., 2002; Tryggvason et al., 2006; Malehmir et al., 2006; Skyttä et al., 2012; Hübert et al., 2009). These metasedimentary rocks are expected to be conductive due to their high content of graphitic metapelites. The fact that the basement is found deeper in our current study

area (about 10 km) than in the western part of the district (4 km, see Hübner et al., 2013) is in good alignment with the proposed crustal detachment by Skyttä et al. (2013), shown in Figure 1.

Conductors CIII, CTV and CTVI are significantly large features extending for more than 6 km with high conductivity ($\geq 100 \Omega\cdot\text{m}$) that connect with the basement. They are fairly vertical, laterally constrained and conductive, with core resistivities below $10 \Omega\cdot\text{m}$, looking like somewhat skewed columns in the model. In the case of CTV and CTVI there are actually two adjacent conductive columns. Considering the steepness, vertical extension and conductivity of these features we are inclined to associate these features with large faults and shear zones in the area, like the Fault Zone Conductors (FZC) in Ritter et al. (2005). The high conductivities could then be caused by either the precipitation of sulphides and/or graphite from the fluids one time present in the faults (Haak et al., 1991), or by the presence of saline fluids in cracks and fractures along the fault (e.g. Pedersen et al., 1992; Linde and Pedersen, 2004). If the enhanced conductivities are indeed related to fault zones, it would be expected that they extend laterally along the fault like planes instead of showing like distinct pillars. A possible explanation for the columnar shape of the anomalies is that they occur at fault intersections. Fault intersections can provide the right conditions for mineralizations by enhancing or limiting fluid flow and, in fact, the majority of VHMS-deposits in the district are spatially related to fault intersections (Bauer et al., 2014). Also, fault intersections are potentially more permeable than single fault zones, and thus, may channelize an increased amount of fluids. It is worth noting that even though the data are very sensitive to these features, in particular to CIII and CTV (see section 6.3), all of them are located at the periphery of the model and hence their size and dimensions are not properly resolved. Therefore, it is also possible that the columnar shape is not really required by the data and more data or forward modelling would be needed for a more detailed assessment.

We suggest that these large conductive features represent extensive structures that impact the study area. They are very steep and plunge towards the center of the area. Being so extensive it would be expected that structures hosting these features would influence surface observations, and indeed, they can be associated with recognized high strain zones or lineaments on the surface. CIII occurs very close to the intersection of the Jörn-Gallejaur and the Maurliden-Finnliden shear zones (J-G and M-F, respectively, see Figure 2). CTV is located close to magnetic lineaments identified as splays from the Deppis-Näsliden shear zone (DNSZ in Figures 1 and 2), a crustal-scale shear zone stretching in northern Sweden for more than 100 km, most probably cutting the crust deeply. CTV might also be related to the proposed crustal

detachment by Skyttä et al. (2013) and inferred to follow the dashed line in Figure 1. CTVI would rise to the surface where Bauer et al. (2013) propose a south-dipping fault to explain a pattern change in the airborne magnetics and geological field observations.

8. Discussion

In the following, we discuss further the interpretation presented of the 3D resistivity model (see the previous section), comparing it with the results from other geophysical studies carried out in the area.

8.1. Seismic reflection

Dehghannejad et al. (2012a) carried out a seismic reflection study comprising three c. 30 km long profiles within the study area. The profiles reveal several structures that support and better define the findings of Bauer et al. (2011) (see section 2). To better compare the outcomes of the MT data with those of the seismic study, Figure 12 shows slices through the 3D resistivity model along the CDP lines of each profile: P1, P2 and P3 (see Figure 2 for their map location). The migrated seismic sections together with their interpretation from Dehghannejad et al. (2012a) are plotted on top. From the figure it can be seen that some reflections coincide with resistivity contrasts, indicating that both methods are sensitive to certain lithological boundaries. These are mostly related to variations between high and intermediate resistivities. Like R6 in P1 and R7 in P2 that are partially following the top of RN, and R40 and R13 in P3 that are constraining the highest resistivities in RC. It is possible that these contrasts are then imaging boundaries between felsic and mafic rocks.

An interesting feature on the seismic profiles is a complex diffraction-reflection pattern at the center of P3 (Figure 12, depth 1.5 - 3 km, between CDP numbers 800 and 1400). Dehghannejad et al. (2012a) speculated that this feature may represent lithological contacts within the Skellefte Group or between this group and its basement. The resistivities of the 3D model do not show a clear relationship with the observed diffractions and reflections, but they do indicate that the basement is more likely to be significantly deeper (at least 8 km depth, see section 7.4). Then, the hypothesis of lithological boundaries within the Skellefte Group is more plausible. Studying the 3D MT model, it is possible to see that the shallower branch of the conductive feature CTII is located just to the east of the seismic profile where the diffractions occur. As previously discussed, the CTII conductor might be related to alteration zones within the Skellefte Group, potentially embedding

mineralization zones. Alteration zones or massive sulphides are not only associated to very low resistivities, but also to significant contrasts in acoustic impedance (Dehghannejad et al., 2012b). Then, it can be speculated that the body or structure causing the high conductivities might be also the cause of the diffraction-reflection pattern.

Also worth noting is that none of the reflections within the seismic profiles cut a high conductivity core from the 3D MT model, while in turn the reflections seem to be interrupted by them. For example, R1 and R2 are truncated by CTV in P3, R4 by CTII in P1, and R9 by CTIV in P2 (Figure 12). This is in agreement with our suggestion of the conductors being associated with subvertical faults. Very steep faults cannot be imaged per se with seismics, but they can be detected by the offsets or segmentation they may cause on less steep structures. Particularly in P3, it is possible to see that reflections R1 and R2, that terminate on CTV, seem to run along enhanced conductivities (30 - 100 $\Omega\cdot\text{m}$). This may indicate that the south-dipping shear zones (R1 and R2) could be connected to a subvertical structure along CTV, not seen by the seismics due to its steepness, that aids or aided fluid transport, hence the lower resistivities. However, it is not certain if R1 and R2 in P3 are interrupted by a structure along CTV or by lack of data since these reflections are at the very edge of the profile. Additionally, the enhanced conductivities along R1 and R2 in P3, do not seem to be associated to the south-dipping reflections in P1, complicating the interpretation.

Furthermore, at two locations reflections occur between a conductor and their suspected surface trace (see section 7), intersecting the inferred fault plane that would connect them (R1, R2 and R3 in P1 on top of CTV east, and R8 in P2 on top of CTIV). However, in both cases the implicated surface traces are not direct observations of faults. CTV is associated to magnetic lineaments which are rather complex and may well be the expression of a deeper structure, while CTIV is aligned with the Vargfors dam. Thus the intersecting reflections do not necessarily refute the suggested subvertical structures and their association to the surface traces, instead they imply that if the subvertical faults do exist, they are interrupted by younger shallower structures, adding a greater level of complexity that cannot be properly resolved with the available studies.

It might be possible to further develop the interpretations here presented by modelling a combination of both seismic and MT data. Another possibility is to try to resolve fault zone geometries associated to magnetic lineaments (like CTV) with constrained potential field modelling. As observed by Haak et al. (1991), the precipitation of graphite in metamorphic environments, can be accompanied by precipitation of magnetic minerals like pyrrhotite and thus may give rise to strong anomalies in both magnetic and electromagnetic

data sets.

8.2. Other geophysical data

Tavakoli et al. (2012a) modelled potential field data along the seismic reflection profiles. Comparing the obtained 2D models of gravity and magnetic anomalies with the 3D resistivity model, it is possible to observe a correlation between the Skellefte Group basalts from the potential field models and some shallow resistors. The correlation is not always very good, in some cases there is a shift in position and in others there are differences in shape or size (García Juanatey, 2012, Paper IV). Later on, Tavakoli et al. (2016b) showed that it was possible to resolve these offsets by re-modelling the potential field data.

Besides potential field data, a considerable amount of geoelectrical and induced polarization data has been acquired in the area (Tavakoli et al., 2012b, 2016a). Most of these studies are too shallow to be comparable with the MT data (≈ 400 m depth), except for a 10 km profile that reaches 1.5 km depth, E1 in Tavakoli et al. (2016a). This profile presents an interesting feature with lower resistivities, V4, interpreted as a graphitic shale and a sulphide mineralization along a faulted contact. A slice of the 3D resistivity model along the profile E1 shows broadly a similar resistivity distribution, although it presents a greater span of resistivity values, both lower and higher than those on E1. V4 from E1 coincides with the enhanced conductivities between the conductors of CTIII in the MT model. One kilometer to the east and 1.5 km to the west, in the direction perpendicular to E1 (i.e. along geological strike), the resistivities drop below $3 \Omega \cdot \text{m}$ as the cores of the CTIII conductors are approached. The geoelectrical data along E1 cannot be used to discern whether the CTIII conductors are indeed separated by higher resistivities, as absolute resistivity values are not always comparable between geoelectrical and electromagnetic methods. However, the interpretation of V4, using only geoelectrical and induced polarization data, supports our interpretation of relatively shallow conductors in the MT model (i.e. CTII, CTIII and CTIV) as faults related to alteration zones potentially hosting mineralizations. Although entrained graphite along the faults might also be a source for low resistivities.

9. Conclusions

Processing, analysis, modelling and interpretation of new broadband MT data has been carried out in an important Palaeoproterozoic mining area. To handle the variable degree of noise in the data, a systematic quality check was performed using component-wise 1D inversions. This procedure was not only

applied to select data suitable for inversion, but was also used to calculate appropriate error floors for the selected data points. The data were inverted in both 2D and 3D, producing consistent resistivity models able to fit the data reasonably well. A comparison between the different models revealed that the 3D model, calculated with the full impedance tensor, was able to fit the data much better than the 2D models obtained with the determinant of the impedance tensor. The 3D model was, thus, further assessed and interpreted in conjunction with already existing geological and geophysical observations in the area. The 2D models served to validate the 3D model and identify robust features in it.

The main geological units in the area were successfully imaged at depth, large and middle sized conductors were found. The depth extension of the Skellefte Group was estimated to be about 10 km, where it meets a more conductive unit. This unit was interpreted as the basement of the district, associated to rocks of the Bothnian Basin. The GI-phase of the Jörn intrusion was depicted to 6 km depth, while the TIB granites down to 5 km. Although the precise source of the extreme conductivities could not be determined, the conductors were interpreted as faults and shear zones. The larger conductors depict crustal-scale features that are more than 6 km long. They surround the study area and connect with the basement. The smaller conductors are embedded within the Skellefte Group rocks, aligning with the geological strike, and were tagged as good candidates for hydrothermally altered zones hosting mineralizations.

Since most of the massive sulfide mineralizations in the Skellefte District are structurally controlled, the fault zones pictured by the MT inversions offer a great opportunity to better investigate the relationship between these structures and the existing mineralizations, The current study already implies that larger structures may have played an important role in the ore formation processes of the area. The better the mineral system is understood, the more successful will the exploration at larger depths and scales may be.

Further modelling and integration of all the already available geological and geophysical data may provide more answers.

Acknowledgments

We thank all project partners for their collaboration and support. We also thank Kristina Juhlin, Jochen Kamm, Tobias Lochbühler and Chunling Shan, for helping to carry out measurements under typical late-October conditions in Norrland. This work was funded by New Boliden and the project “VINNOVA 4D modelling of the Skellefte District”. The manuscript was improved by kind and helpful comments from Benjamin S. Murphy and an

anonymous reviewer. We dedicate this paper to Prof. Laust Børsting Pedersen who left us prematurely in 2017.

References

- Alekseev, D., Palshin, N., and Varentsov, I. (2009). Magnetotelluric dispersion relations in a two-dimensional model of the coastal effect. *Izvestiya Physics of the Solid Earth*, 45:167–170. 10.1134/S1069351309020062.
- Allen, R., Weihed, P., and Svenson, S. (1996). Setting of Zn-Cu-Au-Ag massive sulfide deposits in the evolution and facies architecture of a 1.9 Ga marine volcanic arc, Skellefte district, Sweden. *Economic Geology and the Bulletin of the Society of Economic Geologists*, 91(6):1022–1053.
- Bahr, K. (1988). Interpretation of the magnetotelluric impedance tensor: regional induction and local telluric distortion. *Journal of Geophysics-Zeitschrift für Geophysik*, 62(2):119–127.
- Bahr, K. (1991). Geological noise in magnetotelluric data: a classification of distortion types. *Physics of The Earth and Planetary Interiors*, 66(1-2):24 – 38.
- Bauer, T., Skyttä, P., Allen, R., and Weihed, P. (2013). Fault-controlled sedimentation in a progressively opening extensional basin: the Palaeoproterozoic Vargfors basin, Skellefte mining district, Sweden. *International Journal of Earth Sciences*, 102(2):385–400. Accepted for publication.
- Bauer, T. E., Skyttä, P., Hermansson, T., Allen, R. L., and Weihed, P. (2014). Correlation between distribution and shape of VMS deposits and regional deformation patterns, Skellefte district, northern Sweden. *Mineralium Deposita*, 49(5):555–573.
- Bauer, T. E., Skyttä, P., Allen, R. L., and Weihed, P. (2011). Syn-extensional faulting controlling structural inversion – Insights from the Palaeoproterozoic Vargfors syncline, Skellefte mining district, Sweden. *Precambrian Research*, 191(3–4):166 – 183.
- Berdichevsky, M. N. and Pokhotelov, D. O. (1997). Violation of the Dispersion Relations in a Three-Dimensional Magnetotelluric Model. *Izvestiya Physics of the Solid Earth*, 8:213–243.
- Bergman Weihed, J. (2001). Palaeoproterozoic deformation zones in the Skellefte and the Arvidsjaur areas, northern Sweden. In Weihed, P., editor,

- Economic Geology Research 1*, number 833 in C, pages 46–68. Sveriges Geologiska Undersökning.
- Billström, K. and Weihed, P. (1996). Age and provenance of host rocks and ores in the paleoproterozoic Skellefte district, northern Sweden. *Economic Geology and the Bulletin of the Society of Economic Geologists*, 91(6):1054–1072.
- Cherevatova, M., Smirnov, M., Jones, A., Pedersen, L., Becken, M., Biolik, M., Cherevatova, M., Ebbing, J., Gradmann, S., Gurk, M., Hübert, J., Jones, A., Junge, A., Kamm, J., Korja, T., Lahti, I., Löwer, A., Nittinger, C., Pedersen, L., Savvaidis, A., and Smirnov, M. (2015). Magnetotelluric array data analysis from north-west fennoscandia. *Tectonophysics*, 653:1 – 19.
- Constable, S. C., Parker, R. L., and Constable, C. G. (1987). Occam’s inversion: A practical algorithm for generating smooth models from electromagnetic sounding data. *GEOPHYSICS*, 52(3):289–300.
- Dehghannejad, M., Bauer, T. E., Malehmir, A., Juhlin, C., and Weihed, P. (2012a). Crustal geometry of the central Skellefte district, northern Sweden - constraints from reflection seismic investigations. *Tectonophysics*, 524:87–99.
- Dehghannejad, M., Juhlin, C., Malehmir, A., Skyttä, P., and Weihed, P. (2010). Reflection seismic imaging of the upper crust in the Kristineberg mining area, northern Sweden. *Journal of Applied Geophysics*, 71(4):125 – 136.
- Dehghannejad, M., Malehmir, A., Juhlin, C., and Skyttä, P. (2012b). 3D constraints and finite-difference modeling of massive sulfide deposits: The Kristineberg seismic lines revisited, northern Sweden. *GEOPHYSICS*, 77(5):WC69–WC79.
- Dumas, H. (1986). *Litho-facies of the metasedimentary formations in the central part of the Skellefte District*. Licentiate thesis, Luleå University of Technology, Sweden.
- García Juanatey, M. A. (2012). *Seismics, 2D and 3D Inversion of Magnetotellurics : Jigsaw pieces in understanding the Skellefte Ore District*. PhD thesis, Uppsala University.
- García Juanatey, M. A., Hübert, J., Tryggvason, A., and Pedersen, L. B. (2013a). Imaging the Kristineberg mining area with two perpendicular

- magnetotelluric profiles in the Skellefte Ore District, northern Sweden. *Geophysical Prospecting*, 61(1):200–219.
- García Juanatey, M. A., Tryggvason, A., Juhlin, C., Bergström, U., Hübert, J., and Pedersen, L. B. (2013b). MT and reflection seismics in the north-western Skellefte Ore District, Sweden. *Geophysics*, 78(2):B65–B76.
- González-Roldán, M. (2010). *Mineralogía, petrología y geoquímica de intrusiones sin-volcánicas en el distrito minero de Skellefte, norte de Suecia*. PhD thesis, University of Huelva.
- Haak, V., Stoll, J., and Winter, H. (1991). Why is the electrical resistivity around the KTB hole so low? *Physics of the Earth and Planetary Interiors*, 66(1–2):12 – 23.
- Hübert, J., García Juanatey, M. A., Malehmir, A., Tryggvason, A., and Pedersen, L. B. (2013). The upper crustal 3-D resistivity structure of the Kristineberg area, Skellefte district, northern Sweden revealed by magnetotelluric data. *Geophysical Journal International*, 192(2):500–513.
- Hübert, J., Malehmir, A., Smirnov, M., Tryggvason, A., and Pedersen, L. B. (2009). MT measurements in the western part of the Paleoproterozoic Skellefte Ore District, Northern Sweden: A contribution to an integrated geophysical study. *Tectonophysics*, 475(3-4):493 – 502.
- Kalscheuer, T., De los Ángeles García Juanatey, M., Meqbel, N., and Pedersen, L. B. (2010). Non-linear model error and resolution properties from two-dimensional single and joint inversions of direct current resistivity and radiomagnetotelluric data. *Geophysical Journal International*, 182(3):1174–1188.
- Kathol, B. and Weihed, P. (2005). *Description of regional geological and geophysical maps of the Skellefte District and surrounding areas*. SGU Uppsala.
- Linde, N. and Pedersen, L. (2004). Characterization of a fractured granite using radio magnetotelluric (RMT) data. *GEOPHYSICS*, 69(5):1155–1165.
- Malehmir, A., Tryggvason, A., Juhlin, C., Rodriguez-Tablante, J., and Weihed, P. (2006). Seismic imaging and potential field modelling to delineate structures hosting VHMS deposits in the Skellefte Ore District, northern Sweden. *Tectonophysics*, 426(3-4):319 – 334.

- Parker, R. L. and Booker, J. R. (1996). Optimal one-dimensional inversion and bounding of magnetotelluric apparent resistivity and phase measurements. *Physics of the Earth and Planetary Interiors*, 98(3–4):269 – 282.
- Pedersen, L. and Engels, M. (2005). Routine 2D inversion of magnetotelluric data using the determinant of the impedance tensor. *Geophysics*, 70(2):G33–G41.
- Pedersen, L. B., Juhlin, C., and Rasmussen, T. M. (1992). Electric resistivity in the Gravberg-1 Deep Well, Sweden. *Journal of Geophysical Research: Solid Earth*, 97(B6):9171–9182.
- Ritter, O., Hoffmann-Rothe, A., Bedrosian, P. A., Weckmann, U., and Haak, V. (2005). Electrical conductivity images of active and fossil fault zones. In Bruhn, D. and Burlini, L., editors, *High-Strain Zones: Structure and Physical Properties*, volume 245 of *Special Publications*, pages 165–186. Geological Society, London.
- Rutland, R. W. R., Kero, L., Nilsson, G., and Stølen, L. K. (2001). Nature of a major tectonic discontinuity in the Svecofennian province of northern Sweden. *Precambrian Research*, 112(3-4):211 – 237.
- Siripunvaraporn, W., Egbert, G., Lenbury, Y., and Uyeshima, M. (2005). Three-dimensional magnetotelluric inversion: data-space method. *Physics of the Earth and Planetary Interiors*, 150(1-3):3–14.
- Skyttä, P., Bauer, T. E., Hermansson, T., Dehghannejad, M., Allen, R. L., Juhlin, C., Weihed, P., Tavakoli, S., Hübner, J., and García Juanatey, M. A. (2013). Crustal 3-D geometry of the Kristineberg area (Sweden) with implications on VMS deposits. *Solid Earth*, 4(2):387–404.
- Skyttä, P., Bauer, T. E., Tavakoli, S., Hermansson, T., Andersson, J., and Weihed, P. (2012). Pre-1.87 Ga development of crustal domains overprinted by 1.87 Ga transpression in the Palaeoproterozoic Skellefte District, Sweden. *Precambrian Research*, 206-207:109–136.
- Skyttä, P., Hermansson, T., Andersson, J., and Weihed, P. (2011). New zircon data supporting models of short-lived igneous activity at 1.89 Ga in the western Skellefte District, central Fennoscandian Shield. *Solid Earth*, 2:205–217.
- Smirnov, M. (2003). Magnetotelluric data processing with a robust statistical procedure having a high breakdown point. *Geophysical Journal International*, 152(1):1–7.

- Smirnov, M. Y. and Pedersen, L. B. (2009). Magnetotelluric measurements across the Sorgenfrei-Tornquist Zone in southern Sweden and Denmark. *Geophysical Journal International*, 176(2):443–456.
- Swift, C. M. (1967). *A magnetotelluric investigation of an electrical conductivity anomaly in the southwestern United States*. Thesis, Massachusetts Institute of Technology. Advisor: Theodore R. Madden.
- Tavakoli, S., Bauer, T., Rasmussen, T., Weihed, P., and Elming, S.-Å. (2016a). Deep massive sulphide exploration using 2d and 3d geoelectrical and induced polarization data in skellefte mining district, northern sweden. *Geophysical Prospecting*, 64(6):1602–1619.
- Tavakoli, S., Bauer, T. E., Elming, S.-Å., Thunehed, H., and Weihed, P. (2012a). Regional-scale geometry of the central Skellefte district, northern Sweden - results from 2.5D potential field modelling along three previously acquired seismic profiles. *Applied Geophysics*. Accepted for publication.
- Tavakoli, S., Dehghannejad, M., García Juanatey, M. A., Bauer, T. E., Weihed, P., and Elming, S.-Å. (2016b). Potential field, geoelectrical and reflection seismic investigations for massive sulphide exploration in the skellefte mining district, northern sweden. *Acta Geophysica*, 64(6):2171–2199.
- Tavakoli, S., Elming, S.-Å., and Thunehed, H. (2012b). Geophysical modelling of the central Skellefte district, Northern Sweden; an integrated model based on the electrical, potential field and petrophysical data. *Applied Geophysics*, 82:84–100.
- Tryggvason, A., Malehmir, A., Rodriguez-Tablante, J., Juhlin, C., and Weihed, P. (2006). Reflection seismic investigations in the western part of the paleoproterozoic VHMS-bearing Skellefte district, northern Sweden. *Economic Geology*, 101(5):1039–1054.
- Weidelt, P. and Kaikkonen, P. (1994). Local 1-D interpretation of magnetotelluric B-polarization impedances. *Geophysical Journal International*, 117(3):733–748.
- Weihed, P. (2010). Palaeoproterozoic mineralized volcanic arc systems and tectonic evolution of the Fennoscandian Shield: Skellefte District Sweden. *GFF*, 132(1):83–91.
- Weihed, P., Arndt, N., Billström, K., Duchesne, J.-C., Eilu, P., Martinsson, O., Papunen, H., and Lahtinen, R. (2005). 8: Precambrian geodynamics

- and ore formation: The Fennoscandian Shield. *Ore Geology Reviews*, 27(1-4):273 – 322. Special Issue on Geodynamics and Ore Deposit Evolution in Europe.
- Weihed, P., Billstrom, K., Persson, P., and Weihed, J. (2002). Relationship between 1.90-1.85 Ga accretionary processes and 1.82-1.80 Ga oblique subduction at the Karelian craton margin, Fennoscandian Shield. *Journal of the Geological Society of Sweden*, 124(Part 3):163–180.
- Wiese, H. (1962). Geomagnetische Tiefentellurik Teil II: Die Streichrichtung der Untergrundstrukturen des elektrischen Widerstands, erschlossen aus geomagnetischen Variationen. *Geofisica pura e applicata*, pages 83–103.
- Wilson, M. R., Sehlstedt, S., Åke Claesson, L., Smellie, J. A., Aftalion, M., Hamilton, P. J., and Fallick, A. E. (1987). Jörn: An Early Proterozoic intrusive complex in a volcanic-arc environment, north Sweden. *Precambrian Research*, 36(3-4):201 – 225.
- Yan, P., García Juanatey, M. A., Kalscheuer, T., Juhlin, C., Hedin, P., Savvaidis, A., Lorenz, H., and Kück, J. (2017). A magnetotelluric investigation of the scandinavian caledonides in western jämtland, sweden, using the cosec borehole logs as prior information. *Geophysical Journal International*, 208(3):1465–1489.
- Zhang, P., Roberts, R., and Pedersen, L. (1987). Magnetotelluric strike rules. *Geophysics*, 52(3):267–278.

Site	Zxy	Zyx	Det	Site	Zxy	Zyx	Det
A01	25	4	27	B01	7	5	34
A02	11	13	38	B02	9	13	29
A03	10	4	32	B03	25	64	52
A04	2	2	23	B05	133	*	583
A05	7	3	32	B06	13	111	65
A06	9	5	35	B07	12	17	36
A07	144	64	70	B08	7	5	41
A08	5	4	33	B09	31	16	37
A09	*	6	75	B10	6	6	45
A10	4	3	33	B11	6	4	35
A11	3	8	63	B12	3	2	33
A12	57	*	318	B13	3	7	33
A13	4	3	30	B14	3	3	32
A14	17	31	29	B15	20	10	33
A15	4	3	31	B16	3	3	31
A16	18	*	66	B17	3	3	35
A17	5	3	29	B18	7	3	31
A18	23	2	28	B19	25	42	30

Table 1: RMS obtained from individual 1D inversions of the off-diagonal elements of the impedance tensor and the determinant (assuming relative errors of 1%). For the 3D inversion, the RMS values for Zxy and Zyx were used as error floors for the impedance elements, additionally to a global error floor of 5% and the original errors. For the 2D inversion of the determinant, given the similarity of the obtained values, a single global error floor of 5% was used instead (also in addition to the original errors). Excluded data is marked with a box. Values higher than 1000 are marked with '*'. All showed values are percentages.

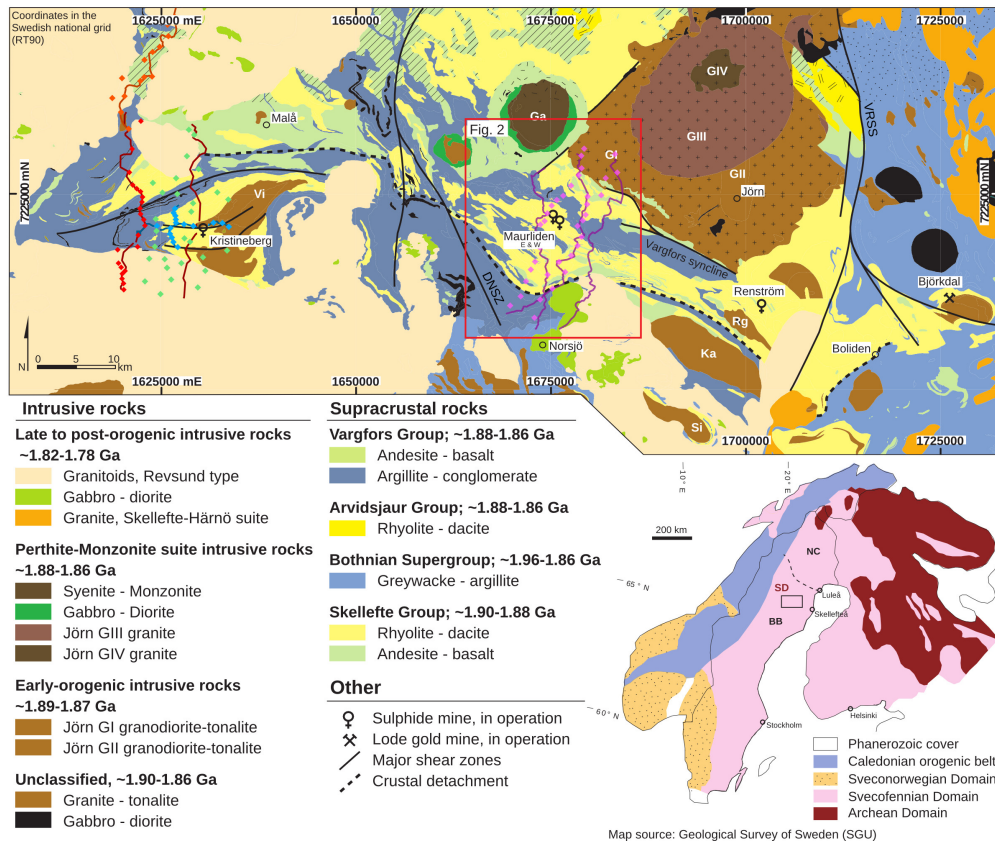


Figure 1: Geological map of the Skellefte District with the location of the MT sites (Hübert et al., 2009, 2013; García Juanatey et al., 2013a,b) and seismic reflection profiles (Tryggvason et al., 2006; Dehghannejad et al., 2010, 2012a; García Juanatey et al., 2013b), different colours indicate different field campaigns. Major shear zones are the north - south trending Däppis-Näsliden shear zone (DNSZ) and Vidsel-Röjnoret shear system (VRSS). Modified after Kathol and Weihed (2005); Bauer et al. (2011), Geological Survey of Sweden (SGU). Inset: Generalized geology of the Fennoscandian shield. Geological domains: BB: Bothnian Basin, NC: Norrbotten Craton. SD: Skellefte district (shown above). The dashed line represents the boundary between rocks with Proterozoic and Archean Nd-signatures (Mellqvist1999). Modified after Weihed et al. (2002).

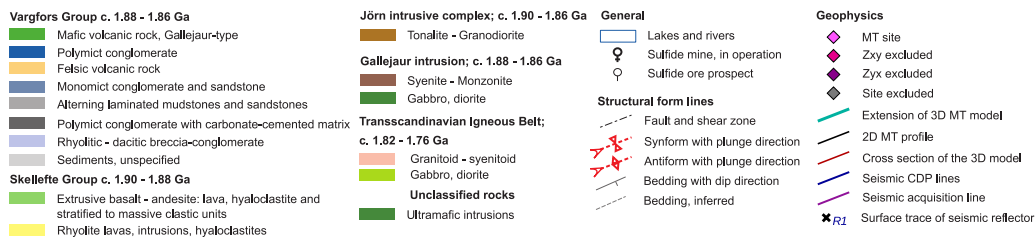
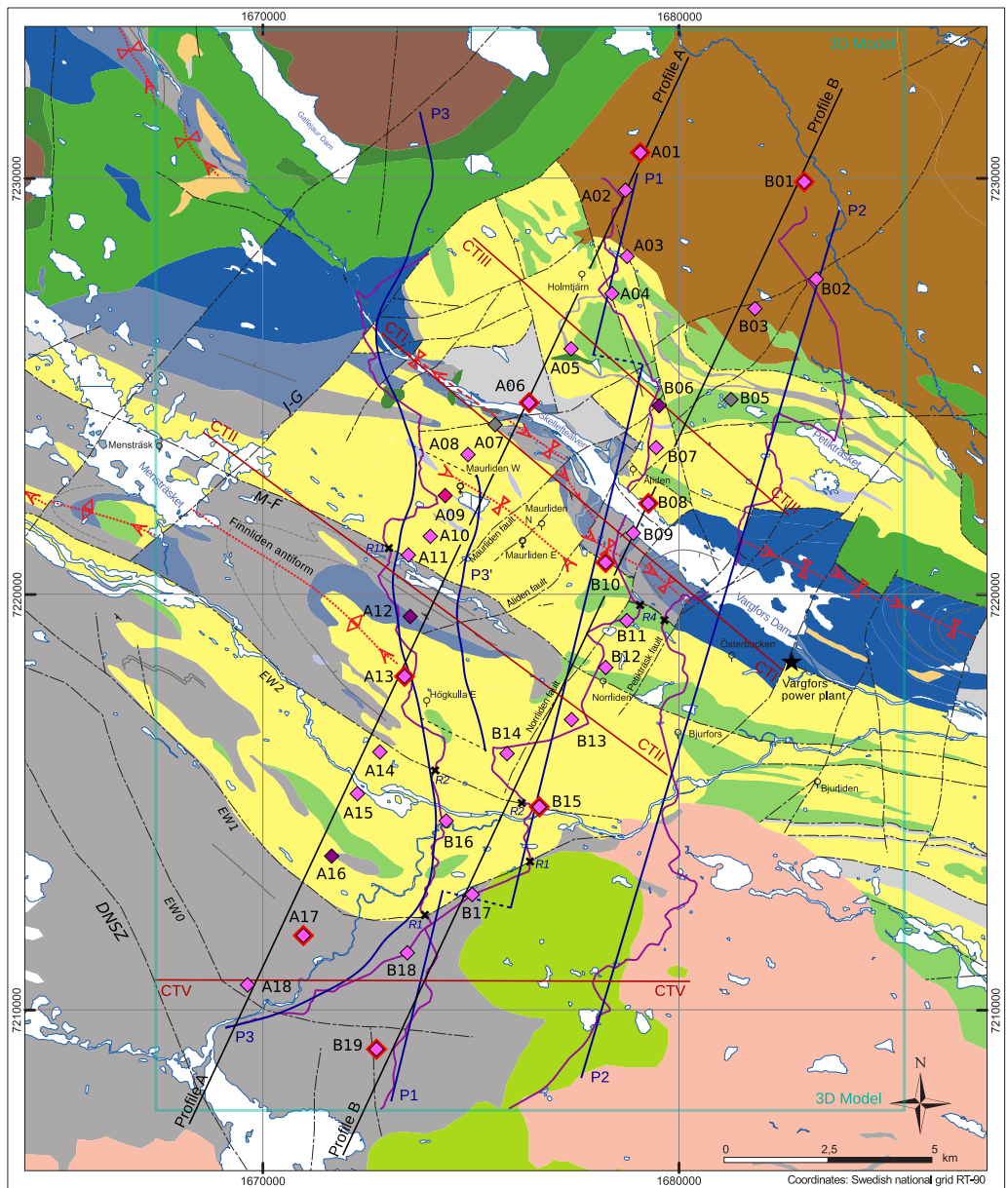


Figure 2: Geological map of the central Skellefte District showing the location of the main geological units, faults and shear zones, MT sites, 2D profiles A and B, and vertical slices of the 3D model shown in Figures 11 and 12. Sites shown in Figure 3 are outlined in red. Modified after Allen et al. (1996), Bauer et al. (2011), Kathol and Weihed (2005), and the Geological Survey of Sweden (SGU).

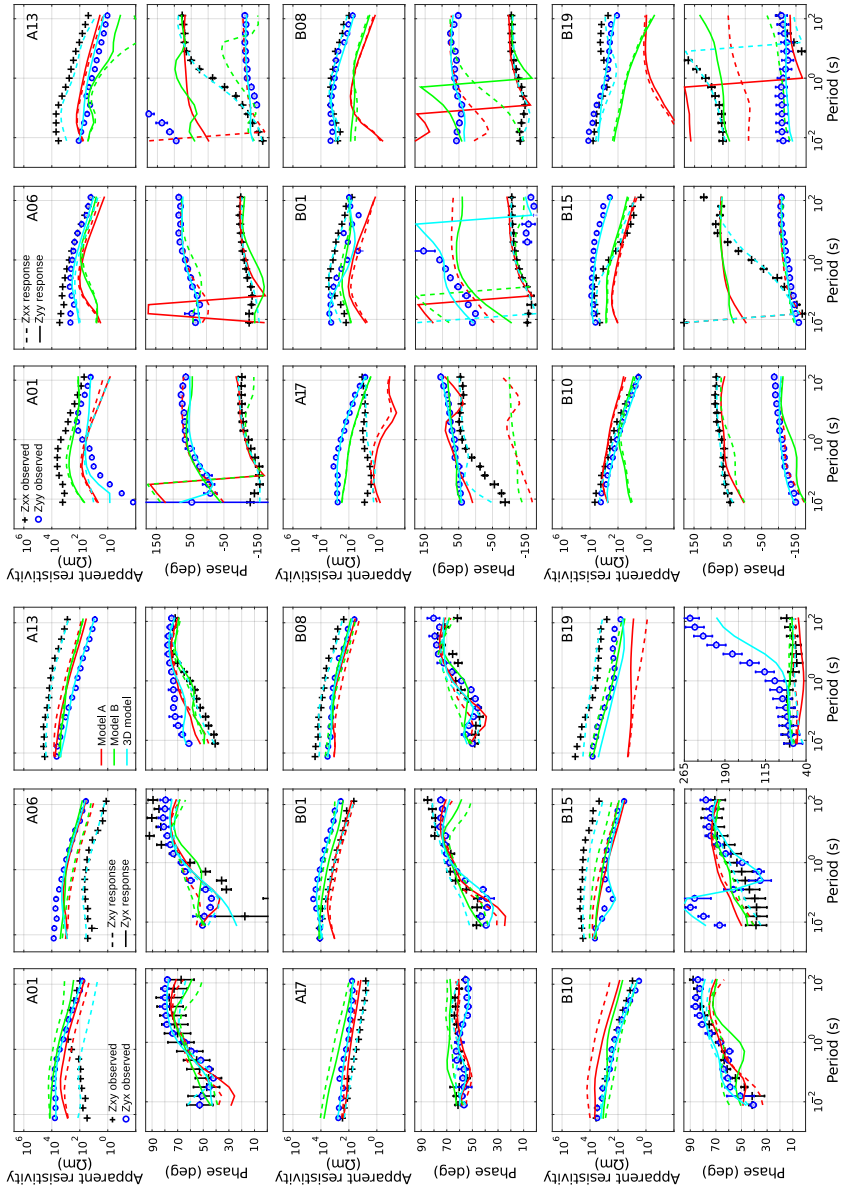


Figure 3: Apparent resistivity and phase of the measured data and model responses for all elements of the impedance tensor of selected sites (highlighted in Figure 2). The red and green lines are the model responses of the 2D models along profiles A and B, respectively. The responses of the 3D model are shown in cyan. Note that the 2D responses are rotated and therefore the diagonal components are also shown. The 3D model shows a better data fit in almost all cases, particularly at site B19 where it reproduces the off-quadrant phases.

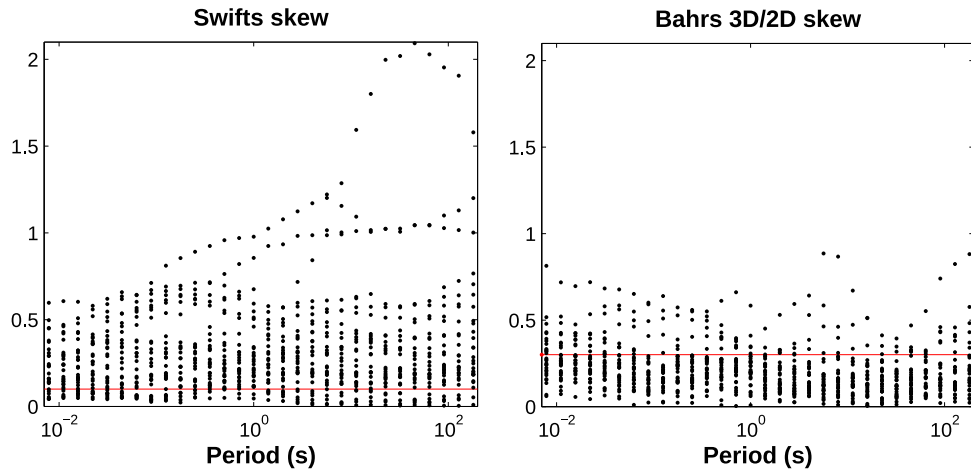


Figure 4: Rotational invariants Swift's and Bahr's 2D/3D skews. The line indicates the proposed thresholds below which the data could be explained with 2D models.

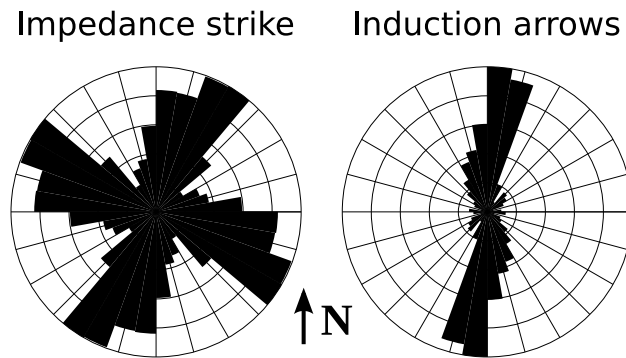


Figure 5: Rose plots indicating the estimated strike angles from the impedance tensor and the orientation of real induction arrows. Note that the calculated strike angles have 90° ambiguity and that in ideal 2D environments, the real induction arrows are perpendicular to the strike.

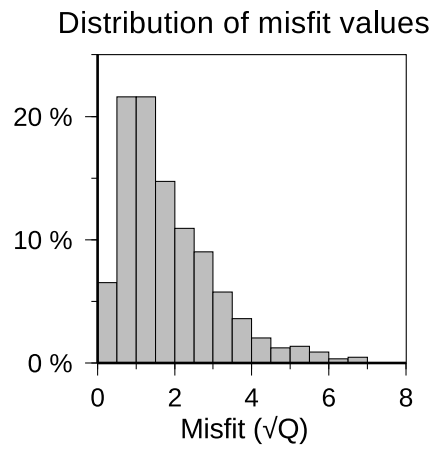


Figure 6: Histogram showing the distribution of misfit values (\sqrt{Q}) for the estimated strike angles from the impedance tensor. A value of one indicates that the impedance tensor fulfills 2D conditions with the assumed errors and strike direction.

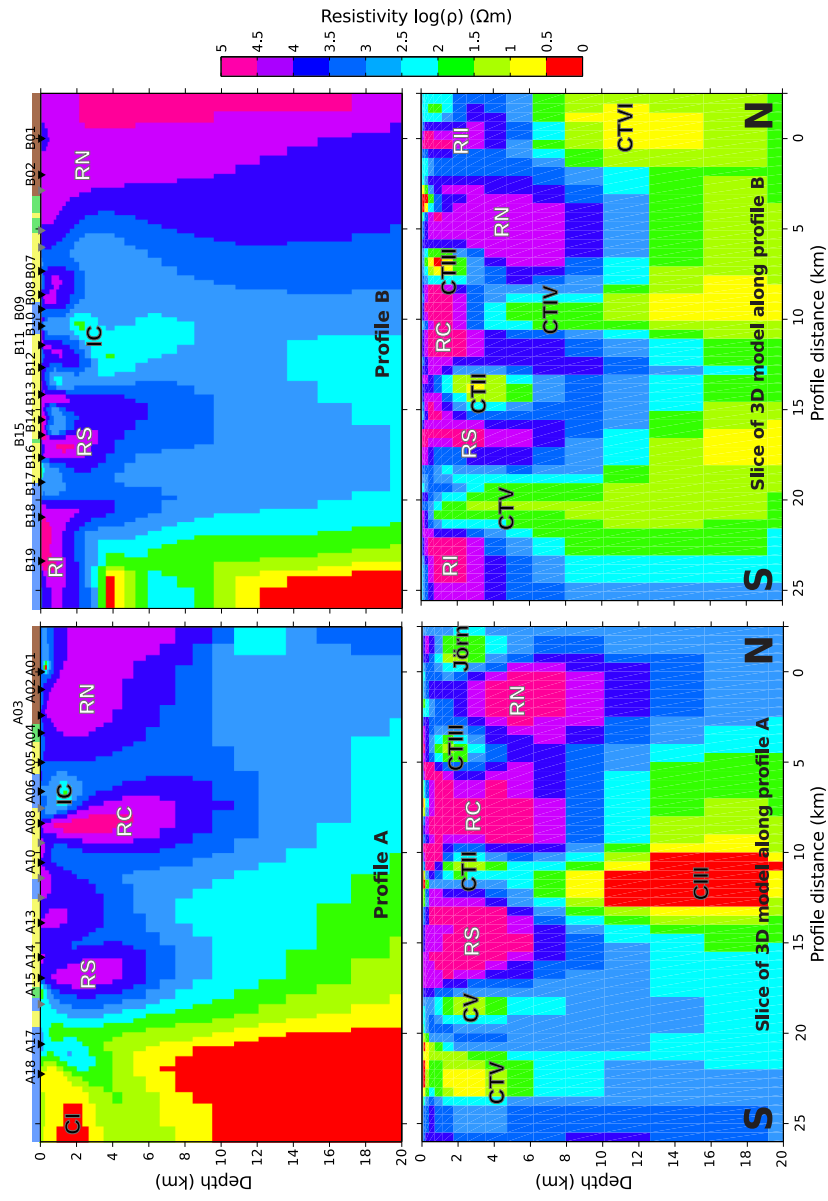


Figure 7: Top: 2D resistivity models. Bottom: vertical slices of the 3D resistivity model along the 2D profiles (see Figure 2 for location). All labelled features are discussed in the text.

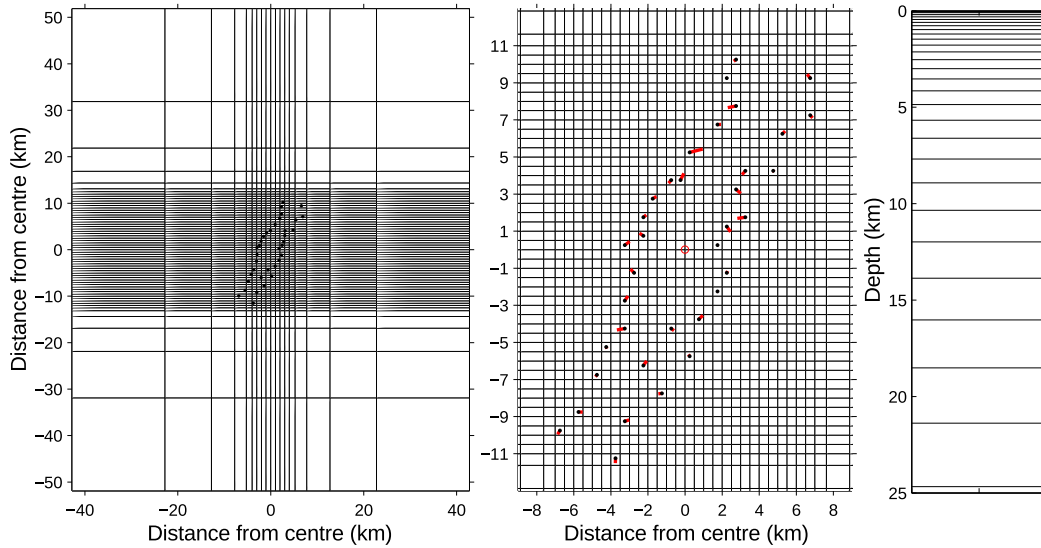


Figure 8: Horizontal and vertical discretization (left and right, respectively) of the 3D resistivity model. Middle figure is a close up of the centre of the model where horizontal cell sizes are equal. Red lines denote how much each site was moved to fit the centre of the cell. In some case sites were moved to an adjacent cell to allow at least one or two free cells between sites.

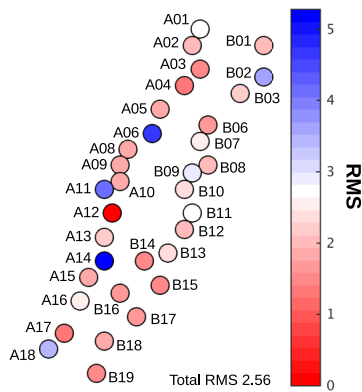


Figure 9: RMS data fit of the 3D model for each site. The colorbar is centered around the total RMS of the 3D model (2.64). The RMS distribution does not evidence a geographical bias, overfitted or underfitted sites do not cluster.

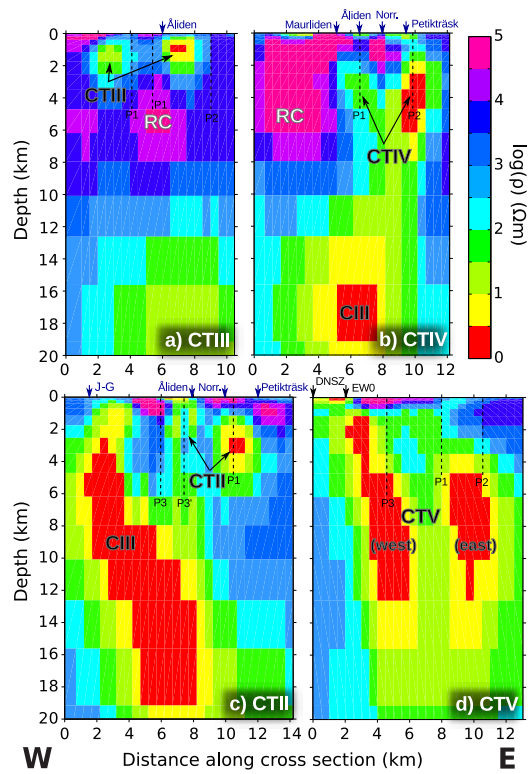


Figure 11: Vertical slices of the 3D model across main trends of conductors (see Figure 2 for location). Dashed lines indicate the location of the slices along seismic CDP lines in Figure 12. Arrows at the surface indicate the location of faults striking NE-SW in blue, and NW-SE in black. Fault names are also shown in Figure 2.

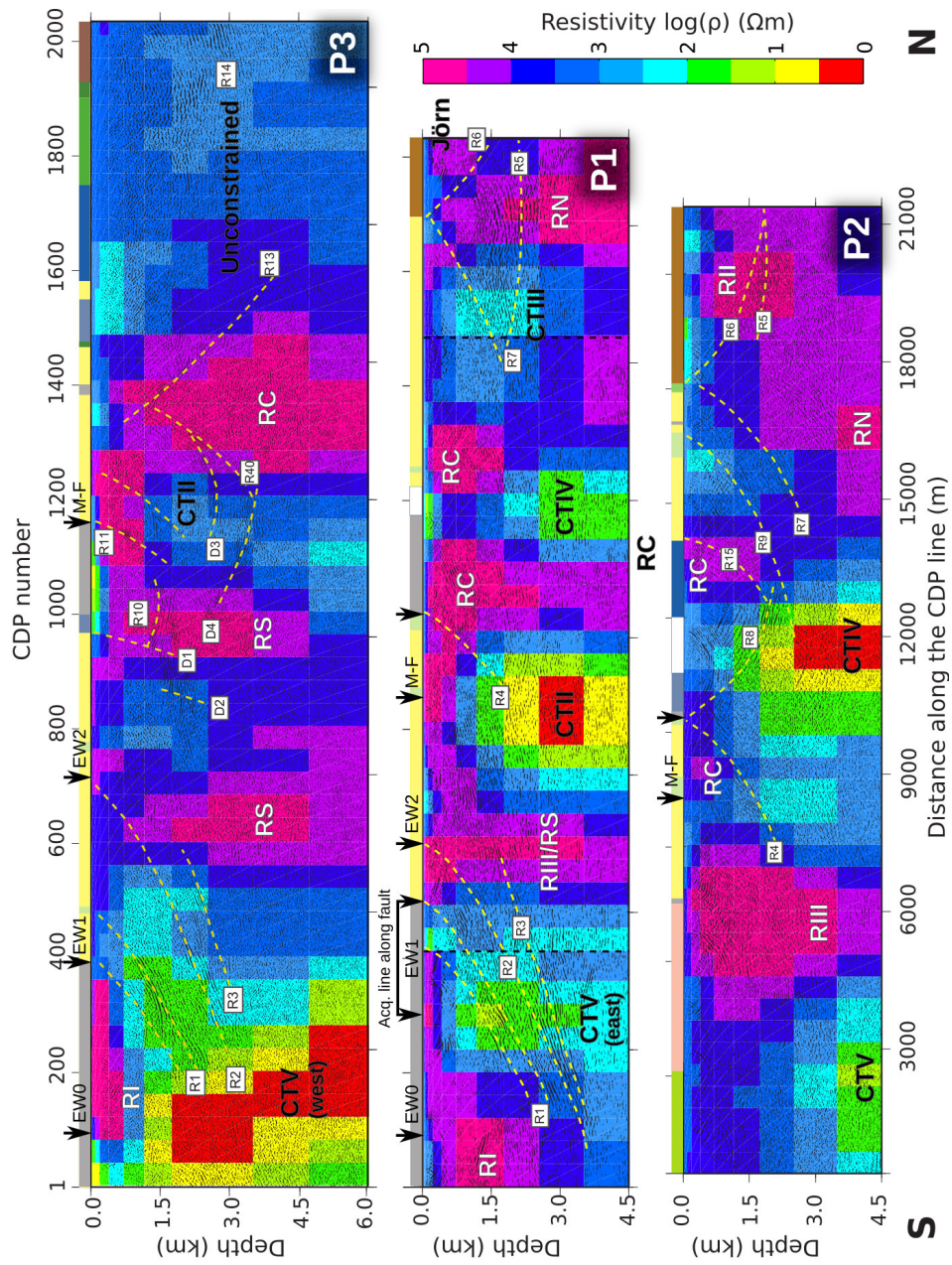


Figure 12: Slices of the 3D resistivity model along the CDP lines showing the migrated seismic reflection section. The interpretation of Dehghannejad et al. (2012a) is shown as yellow dashed lines. Arrows and colours at the surface indicate the surface traces of faults and lithological units along the seismic acquisition lines. See text for discussion and Figure 2 for location.